

High entropy modulated quantum paraelectric perovskite for capacitive energy storage

Received: 3 December 2024

Accepted: 10 April 2025

Published online: 23 April 2025



Yongbo Fan¹, Wanbo Qu², Haifa Qiu¹, Shuaibing Gao³, Lu Li¹, Zezhou Lin¹, Yuxuan Yang², Junyi Yu^{4,5}, Lin Wang⁴, Saiwei Luan⁴, Hao Li¹, Lin Lei⁶, Yang Zhang⁷, Huiqing Fan⁶, Haijun Wu²✉, Shuhui Yu^{4,5} & Haitao Huang¹✉

Electrostatic capacitors are critical components in the power system of electric vehicles (EVs). The current commercially available solutions are largely based on ferroelectric oxides of which the permittivity decrease with increasing electric field. Here, we propose a high entropy modulation design in a quantum paraelectric-ferroelectric/antiferroelectric matrix, which enables a stable and field-independent energy charge/discharge response across a wide voltage range. By effectively synergizing the high efficiency (η) of quantum paraelectrics and the high polarization of the ferroelectric/anti-ferroelectric matrix with the entropy regulator, a high recoverable energy density (W_{rec}) of 13.3 J cm^{-3} with an η of 92.4% is achieved in the bulk state of the perovskite material, promising for device scale-up. Versatile polar regions as well as a defect-less microstructure is achieved by the optimized compositional design and material processing. On a mesoscopic level, the electrical microstructure of the material is engineered to provide a large breakdown strength (E_b) of 750 kV/cm , which is confirmed by the resolved electrochemical information and finite-element simulation. The proposed strategy provides a new path for designing high performance next generation energy storage/power converting dielectrics. This demonstration of quantum paraelectrics for energy storage application is expected to stimulate extensive efforts in the area.

Recently, increasing attention has been paid to electrostatic energy storage due to its extraordinary functional performance resulting from its swift response time ($\sim \text{ns}$) towards electric field. Dielectric devices with such performance are widely applied in electrical and electronic devices, for instance, the traction inverter and DC-DC/DC-AC converters onboard electric vehicles (EVs). With the revolution of automobile industry from fossil fuel dependent towards fully electrification, the

optimization of electrical properties of the functional material applied in these critical components would have an increasingly large impact on the general public. A schematic illustration of the dielectric energy storage process and the associated performance is shown in Supplementary Fig. 1. High entropy perovskite is a focus for researches on next generation energy application¹. Attempts to optimize their electrical performance has been made by optimizing the dielectric relaxation

¹Department of Applied Physics, The Hong Kong Polytechnic University, Kowloon, Hong Kong, China. ²State Key Laboratory for Mechanical Behavior of Materials, Xi'an Jiaotong University, Xi'an, China. ³School of Advanced Materials and Nanotechnology, Xidian University, Xi'an, China. ⁴Shenzhen Institute of Advanced Technology, Chinese Academy of Sciences, Shenzhen, China. ⁵University of Chinese Academy of Sciences, Beijing, China. ⁶State Key Laboratory of Solidification Processing, School of Materials Science and Engineering, Northwestern Polytechnical University, Xi'an, China. ⁷Electronic Materials Research Laboratory (Key Lab of Education Ministry), School of Electronic and Information Engineering, and Instrumental Analysis Center, Xi'an Jiaotong University, Xi'an, China. ✉e-mail: wuhaijunnavy@xjtu.edu.cn; aphhuang@polyu.edu.hk

time, relaxation type, crystallization, polar topologies, etc.^{2–6}. An antiferroelectric-ferroelectric perovskite superlattice was constructed to achieve large energy storage density in an integrated on-chip microcapacitor⁷. Entropy modulation is proven successful in stabilizing the crystal structure and achieving superior energy storage performance in bismuth layered dielectrics^{8,9}. Configurational order is proven to be critical in tuning both room temperature and high temperature (> 200 °C) conductivity of electronic materials¹⁰. There are also reports that the transport behavior of carriers is of importance to the device performance^{11–13}. We showcase here that these important aspects for achieving high energy storage performance could be optimized coordinatively by optimizing the electrical microstructure of the dielectric, i.e., the electrical modulus of the insulating components within the material, to achieve superior functional performance in dielectric materials.

Relaxor ferroelectrics has been the focus of developing high energy storage dielectrics due to the highly mobile polar nano region (PNR) which is field-sensitive and give the material its high energy storage efficiency (η)¹⁴. The dynamics and manipulation of PNR has been a focus of many recent studies¹⁵. A wide range of characterization techniques has been applied to fully understand their properties and the underlying mechanisms^{16,17}. PNRs have been observed in a range of oxides with superior energy storage performance, including perovskites and tetragonal tungsten bronzes^{18,19}. Computational approaches are exploited to locate superior performances based on PNR dynamics²⁰. It is widely accepted that the introduction of PNRs rather than ferroelectric domains in inorganic dielectric materials is a prerequisite in achieving high energy storage density (W_{rec}) and η simultaneously²¹. However, the PNR dynamics in high entropy modulated materials still lacks understanding²². This work provides insight with atomic scale high resolution microscopy to address this issue.

Electrical microstructure investigation based on impedance spectroscopy (IS) is widely used to study various energy storage and dielectric material systems^{23,24}. In oxide materials, there are in-depth investigation on BaTiO₃ (BT), Na_{0.5}Bi_{0.5}TiO₃ (NBT), Li₇La₃Zr₂O₁₂ etc^{25–27}. However, the electrical microstructure is hardly resolvable in most newly developed dielectrics, with a single overlapping Debye peak for the imaginary part of electrical modulus (M'') and impedance (Z''), except in the most commercially valuable and widely investigated BT^{28,29}. In this work, the electrical microstructure of NaNbO₃ (NN) based perovskite is resolved for the first time, showing similarity to that of BaTiO₃ based material, verifying the potential of the reported composition as the next generation energy storage dielectric. With appropriate electrode configuration, the electrical microstructure of other dielectrics, semiconductors and battery materials could also be resolved by analyzing the IS data in a similar manner^{30,31}. The technique is also useful in optimizing performance of wearable electronics such as flexible pressure sensors and radio-frequency components^{32,33}.

Currently, NN based composition is under intense development around the world as an alternative to the widely applied BT and (Pb, La) (Zr, Ti)O₃ (PLZT) based compositions for energy storage ceramic capacitors^{34–39}. The similarity in crystal structure and field induced phase transition characteristics of NN based antiferroelectrics with that of PLZT has attracted wide interest from both scientific community and industry^{35,40}. SrTiO₃ (ST) based multilayer ceramic capacitor (MLCC) is a preferred option in high-end market due to its high performance and excellent reliability⁴¹. ST has been used to enhance reliability and thermal stability in some relatively conductive material systems such as BiFeO₃ and NBT based perovskites^{42,43}. Combining the high breakdown strength (E_b) of ST and the high polarization of NN, we used NN-ST as our base material for optimization. Ta⁵⁺ is used to tune the field induced phase transition and enhance the E_b of the niobate^{44,45}. Ca²⁺ is a common dopant in Class I MLCC in tuning the Curie temperature and dielectric performance of the material⁴⁶. Although the quantum paraelectric ST was discovered decades ago,

tuning of its induced ferroelectricity for applications in electrical/electronic systems is still fervently researched^{47–50}. Moreover, Hf⁴⁺, Zr⁴⁺, and Sn⁴⁺ are used in the same stoichiometry as a high entropy modulator to induce high lattice distortion and disorder for enhanced response speed towards external applied electric field. With these considerations, finally, we designed and fabricated (0.75- x)NaNbO₃-0.10NaTaO₃-0.15SrTiO₃- x Ca(Hf _{$x/3$} Zr _{$x/3$} Sn _{$x/3$})O₃ (NN- x CHZS; x = 0.00, 0.02, 0.05, 0.10) ceramics, of which x = 0.10 shows excellent energy storage performance, demonstrating the effectiveness of our design strategy. With this high entropy modulation, the composition is successfully tuned from medium entropy (ME) to high entropy (HE). Configuration entropy is evaluated based on molar fraction of different species (supporting information). This high-performance high entropy composition is unique and of importance from chemical perspective as well, since it is very difficult to achieve single-phase in oxide materials when configuration entropy is high ($\geq 1.5 R$)⁵¹.

Our design strategy and its effects are summarized in Fig. 1. Notably, this is the first work to regulate the dielectric energy storage performance of quantum paraelectrics with high entropy strategy. We start the optimization by using a quantum paraelectric-ferroelectric/antiferroelectric matrix (Fig. 1a). Through entropy engineering, the atomic-level microstructure of the material is significantly changed with higher fluctuation on the B-site of the perovskite (Fig. 1b). The transport behavior is systematically optimized both from the viewpoints of real space and electronic band structure (Fig. 1c, d). The height and density of transport barriers are increased with elevated activation energy (E_a) (Fig. 1c). The band gap is increased based on both experimental results and density function theory (DFT) calculations (Fig. 1d). Thus, E_b of the material is significantly improved as proved by experiments and simulations (Fig. 1b, g). A self-assembled superstructure associated with oxygen octahedral tilting (Fig. 1e) facilitates the field-independent dielectric response. Based on Gibbs free energy equations from Landau's theory, the tilting angle is an order parameter which contribute to the total energy through the coupling terms⁵²: $\beta_1(\theta_1^2 + \theta_2^2 + \theta_3^2) + \beta_{11}(\theta_1^4 + \theta_2^4 + \theta_3^4)$ where β_1 and β_{11} are the octahedral torsion coefficients. A high degree of octahedral tilting induces high torsion stress, and correspondingly high energy of the crystal structural mode. In other words, the octahedral tilting stabilizes the crystal structure by squeezing the dimension of the lattice, lowering the symmetry and creating stronger Nb-O bonds, which absorb the electric energy upon the application of electric field. With such distortion, it takes up more energy for the lattice mode to transform from random/weakly polarized into a highly polarized one, the field induced polarization with such tilting is also reduced. Finally, the electrical microstructure experiences one order of magnitude enhancement in shell modulus with the entropy engineering (Fig. 1f). As a result, the significantly optimized performance enables higher rated voltage for electronics and electrical systems, for example, DC-AC converter and traction inverters for on-board electrical vehicles (EVs) to enable faster charging and high energy utilization efficiency (Fig. 1g)⁵³. With the above illustration, a strategy for quantum paraelectric structural stabilization and high entropy modulation to achieve high energy storage performance and ideal field response is successfully developed and validated in a model dielectric. Detailed analyses of the experimental results validating this design strategy are given below.

Results and discussion

Energy storage performance

Under the guidance of our proposed high entropy modulation method, we successfully fabricated bulk material with both high W_{rec} and excellent η . The high voltage behavior of NN- x CHZS is shown in Fig. 2. As the high entropy modulator is doped into the crystal lattice, the field-dependent behavior of polarization is significantly changed. Namely, the response becomes more linear with the doping (Fig. 2a).

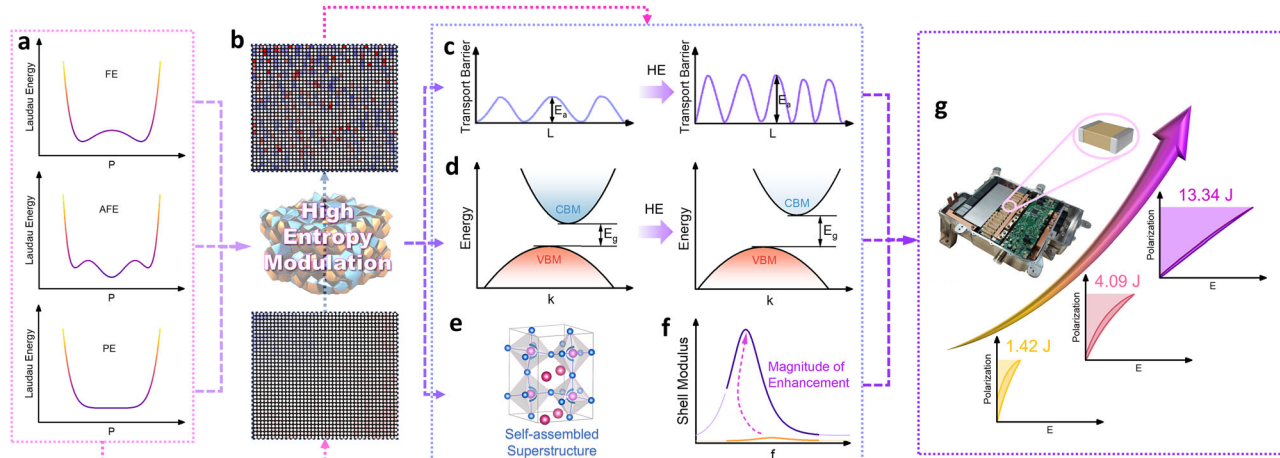


Fig. 1 | Schematic diagram of high entropy modulation in the quantum paraelectric-ferroelectric/antiferroelectric matrix. **a** Landau energy profile of the matrix components. Comparative display of the **(b)** intensity mapping of B-site of the perovskite at atomic scale; **c** height and density of transport barriers along electric field direction L , with E_a being the activation energy of charge carriers; and **(d)** band structure based on experiment and density function theory (DFT)

calculation, highlighting the conduction band minimum (CBM), valence band maximum (VBM) and band gap energy (E_g). **e** Self-assembled twofold crystal superstructure of NN- x CHZS. **f** Electrical microstructure enhancement of one order of magnitude. **g** Elevated operating voltage and energy density of capacitors for traction inverter in electric vehicles (EVs) with the high entropy modulation approach.

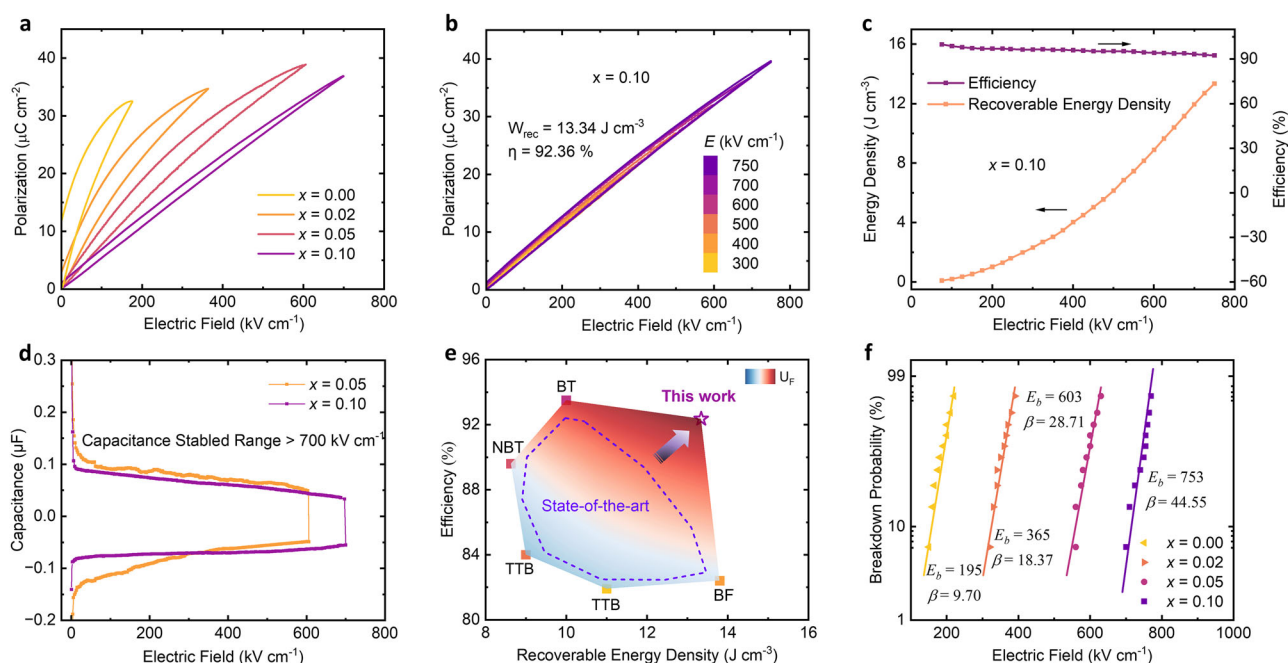


Fig. 2 | Energy storage performance of NN- x CHZS ceramics. **a** P - E loops slightly below E_b . **b** Field-dependent P - E loop for $x = 0.10$. **c** Field-dependent energy storage performance of $x = 0.10$. **d** Comparison of field-dependent capacitance of capacitors made with $x = 0.05$ and 0.10 in the same geometry. **e** Comparison of energy

storage performance (W_{rec} , η and U_F) of NN- x CHZS with current state-of-the-art bulk energy storage dielectrics^{11,18,19,54,75}. **f** Weibull distribution analyses for evaluating the E_b of NN- x CHZS ceramics.

The material can withstand higher electric field with increasing x , while the maximum polarization value of each composition remains on the same level. We adopt the parameter U_F ($=W_{rec}/1-\eta$), as an overall performance indicator for energy storage dielectric³. With our strategy applied, tremendous enhancements in η , W_{rec} and U_F are seen in the NN based dielectric, with an increase of twofold, ninefold, and 55-fold, respectively (Supplementary Fig. 2). These performance indicators of our composition show significant advancements compared with the state-of-the-art of bulk inorganic dielectrics (Fig. 2e). The optimal performance is achieved when $x = 0.10$, of which the η remains steady above 92 % and shows little decay up to 750 kV/cm (Fig. 2b, c). The

capacitance across a wide voltage range is successfully stabilized with the high entropy modulation (Fig. 2d). Based on Weibull analyses for the E_b of NN- x CHZS (Fig. 2f), the statistical value of E_b of the ceramics shows a remarkable improvement from 195 to 753 kV/cm with increasing high entropy modulation, and the reliability of the ceramics is also elevated as reflected by the increased Weibull modulus β from 9.70 to 44.55. We note here that only with a high E_b , a high W_{rec} is achievable, as the case shown in $x = 0.10$. It could be seen from the P - E loops that under the same field of ~ 100 kV cm^{-1} , the W_{rec} values are similar with or without the high entropy modulator (Fig. 2a). However, $x = 0.00$ breaks down before it could reach higher electric field, thus

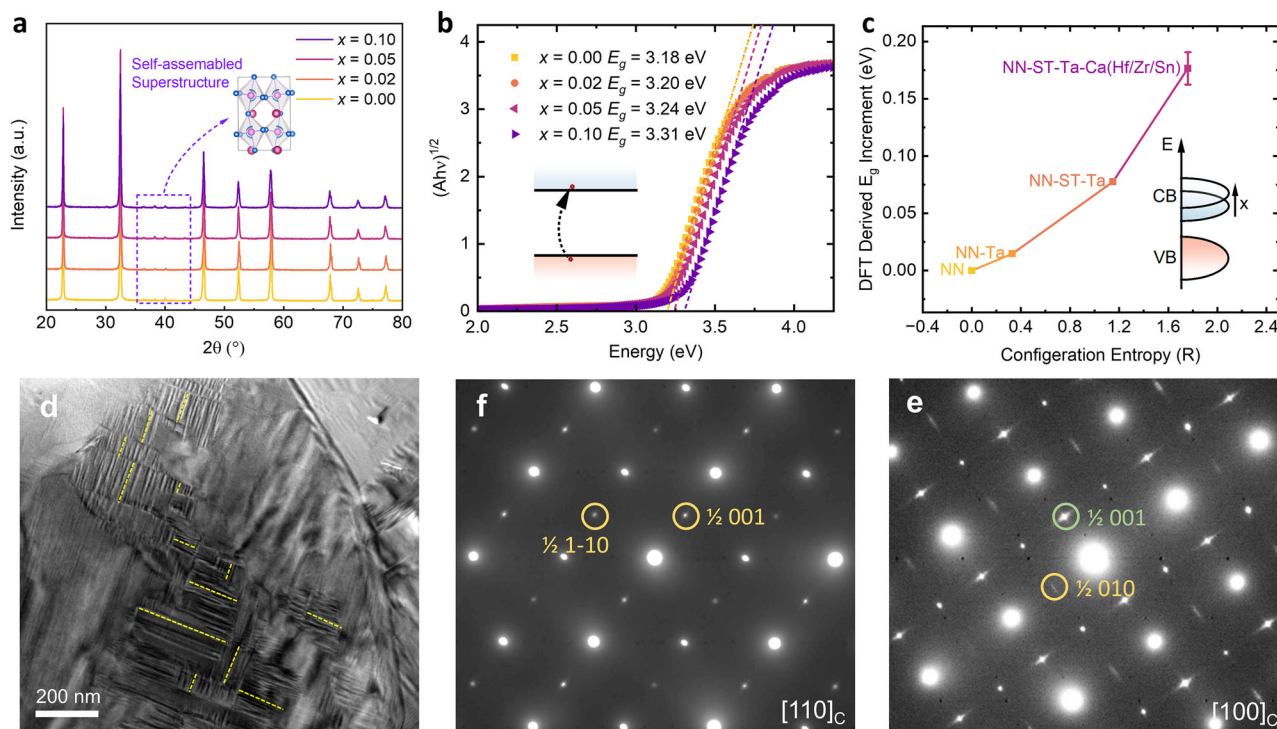


Fig. 3 | Crystal structure, band structure and domain structure of NN-xCHZS ceramics. **a** XRD patterns of NN-xCHZS ceramics. Inset is a schematic of the long range ordered antiferrodistortive structure which gives rise to the distinctive superlattice peaks. **b** Tauc plots of NN-xCHZS derived from the UV-Vis spectrums, with the x -intercept being the indirect band gap (E_g) values. Inset shows the schematic of the activation of electron from valence band (VB) to conduction band (CB).

c DFT derived E_g increment with regard to configuration entropy of NN-xCHZS. Inset shows the schematic variation in band structure. **d** Bright field TEM image of $x = 0.10$, where stripe-like domain features are indicated with yellow dashed lines. SAED images of $x = 0.10$ viewed along the (e) $\langle 110 \rangle_c$ and (f) $\langle 100 \rangle_c$ zone axes. The superlattice diffraction spots confirm the $P2_1ma$ superstructure observed in the XRD diffraction pattern.

couldn't show higher W_{rec} . The reliability of NN-xCHZS is further confirmed by time and field-dependent leakage current measurements. As shown in Supplementary Fig. 3, the leakage current at 100 kV/cm decreases to $\sim 10^{-10}$ A/cm² with increasing x , and is stable with time.

Crystal structure, entropy modulation, and polarization configuration

To illustrate the microscopic origin of the ultrahigh energy storage performance of NN-xCHZS, their polar feature and crystal structure are investigated with transmission electron microscopy (TEM) and X-ray diffraction (XRD). The average crystal structure shows orthorhombic symmetry, while a long-range oxygen octahedral tilting order gives rise to several distinctive superstructure peaks (Fig. 3a). In the below discussion of TEM results, we adopt a pseudocubic indexing for simplicity and without bringing about further confusion, as done by many others^{18,54}. There are no macroscopic domains present in the material, only certain strip-like features with size of tens of nanometers detected under bright field TEM (Fig. 3d). A few dislocations are detected in the grains of $x = 0.10$, which may be caused by entropy associated compositional disorder (Supplementary Fig. 4a). The superstructure is confirmed by selected area electron diffraction (SAED) with $1/2(010)$, $1/2(001)$ superlattice diffraction spots and $1/2(1-10)$, $1/2(001)$ superlattice diffraction spots shown along the zone axes of $\langle 100 \rangle_c$ and $\langle 110 \rangle_c$, respectively (Fig. 3f, e and Supplementary Fig. 4b, c). With precise compositional design based on a holistic consideration of crystal chemistry, structure tolerance, configuration entropy and electronic band structure, we are able to preserve such superstructure despite the high volume of doping ($S_{config} = 1.87$ R). Based on the TEM diffraction pattern, unit cell doubling along at least two crystal directions are present in the material. With this information, the space

group and type of tilting is further identified with Rietveld refinement to be $P2_1ma$ and $a^-b^+c^-$ in Glazer notation, respectively (Supplementary Fig. 5). The information of the $P2_1ma$ space group used in the Rietveld refinement and the refined cell parameters are shown in Supplementary Tables 1 and 2, respectively⁵⁵. The average tilting degree of the oxygen octahedral ω ($\omega = 180^\circ - \angle B-O-B$)/2) in $x = 0.10$ is 8.86° , which is on the same level as pure NN^{36} . The high magnitude of oxygen octahedral tilting serves as a regulator under high electric field. Qi et al. suggested that the tilting angle changes with electric field, absorbing electrical potential energy, stabilizing the crystal structure, thus delaying the polarization saturation up to a higher electric field³⁶. Such characteristics effectively enhance the energy storage density by allowing a continuously rising polarization across a wider applied voltage range⁵⁶. The indirect band gap (E_g) values determined by UV-Vis spectroscopy suggest that the E_g of NN-xCHZS can be effectively tuned from 3.18 to 3.31 eV with the high entropy modulation (Fig. 3b). A higher E_g corresponds to fewer amount of charge carriers stimulated by external factors (electric field, temperature, etc.) and causes lower leakage current during the operation of a dielectric device.

In the temperature dependent permittivity spectrum (Supplementary Fig. 6), the absence of ferroelectric-paraelectric phase transition throughout the entire temperature range, especially at the temperatures approaching 0 K where quantum fluctuation predominates, confirms the quantum paraelectric nature of NN-xCHZS^{57,58}. No deviation from the relationship of $1/\epsilon = A + BT^2$ (A and B are constants, and T is temperature) is detected in NN-xCHZS down to 12 K, suggesting that the quantum critical temperature of this material is below this temperature (Supplementary Fig. 6 inset)⁵⁹. As temperature is decreased, the ferroelectric phase is first suppressed by the strong antiferrodistortion which is visible at room temperature as XRD

and TEM analyses suggested, and is then suppressed by quantum fluctuation until near 0 K⁶⁰.

Since no phase transition is present in NN-*x*CHZS from -0 K to room temperature, there would only be a limited degree of structure distortion across this temperature range, whereas the symmetry of the material would remain unchanged⁶¹. The band structure from DFT calculation suggests that the material has an indirect band gap between the valence band maximum (VBM) located at the Γ (0, 0, 0) point of the Brillouin zone and the conduction band minimum (CBM) near the Z (0, 0, 0.5) point, consistent with experimental results from UV-Vis spectroscopy (Supplementary Figs. 7 and 3b). The conduction band and valence band are dominated by the Nb 4*d* and O 2*p* states, respectively (Supplementary Fig. 7). The Nb 4*d* - O 2*p* orbital hybridization is regarded as a driving force for polar distortion in NN with ionic shift between Nb and O. Incorporating different metal atoms with varied electronegativity and valence electrons destabilizes this hybridization, resulting in changes of the distorted local structure of NbO₆ octahedral and shift in the TM-O ionic bonds, which increases the Nb 4*d* - O 2*p* orbital repulsion, thus heightening the orbital energy near CBM. Upon the dual co-doping of only Sr and Ti, the crystal structure (Supplementary Fig. 8a) has both ferroelectric and antiferroelectric distortions for the neighboring unit cells along *c* direction. Upon the triple co-doping of Sr, Ti, and Ta, the antiferroelectric pattern along *a/b* direction dominates (Supplementary Fig. 8b). Finally, the antiferroelectric ordering becomes more prominent upon high-entropy co-doping of Sr, Ti, Ta, Ca, and Hf/Zr/Sn (Supplementary Fig. 8c-e), which shows the most notable E_g increment (Fig. 3c). Importantly, the calculated increments agree well with the experimental values (Fig. 3b). Our results provide another example of good functionality induced by the competition between ferroelectric and antiferroelectric ferroic orderings other than the recently reported one in NN based system⁶². Recent experimental evidence on crystallographic information suggests that the A site ions in alkali niobates would hybridize with oxygen even without the presence of Pb²⁺ and Bi³⁺, which is in line with our DFT calculation results, suggesting the unique structure of NN may enable better functionality than currently exploited, stemmed from its spontaneous polarization and electrical-mechanical coupling⁶³. With that, the crystal structural origin for the long-range unit cell doubling of octahedral tilting as observed in XRD and TEM data, as well as the band gap increment is revealed. This proves the success of our modulation strategy, since band gap is the intrinsic dominating factor for E_b , and as a result, energy storage performances. Based on DFT calculation, we successfully identified the origin of the enhanced dielectric response, which is the lattice distortion upon the addition of the high entropy modulator and the associated band structure evolutions (Supplementary Figs. 7 and 8). The increase in band gap result in a higher breakdown strength. These mechanisms are confirmed by band gap measurement using UV-Vis spectroscopy and atomic scale microscopy (Figs. 3 and 4).

With the scale of domains down to nanometers suggested by regular TEM, the nature of polar structure in this unique type of quantum paraelectric needs to be investigated at a finer scale. Thus, the atomic level microstructure and corresponding polarization configuration are probed with high-angle annular dark-field scanning transmission electron microscopy (HAADF-STEM) and resolved with customized image recognition computer software package (Fig. 4). Clear image with atomic level resolution is achieved, where the sites with large contrast are identified as dopant sites, i.e., heavier atoms showing brighter contrast, while lighter atoms showing darker contrast (Fig. 4a-c). An even distribution of dopants is present in the sample both on an atomic scale and a mesoscale scale as suggested by HAADF intensity mapping and energy dispersive X-Ray analysis (EDX) mapping analyses (Fig. 4b, c and Supplementary Fig. 9), respectively. The structural distortion associated with the high entropy modulation is found to be distributed evenly across the crystal lattice of *x* = 0.10

(Fig. 4d, e). A-A and B-B bond lengths are found to be fluctuating in a range between 99.3–100.8% and 99.5–100.5% of their average bond lengths, respectively. The mapping of polar vector of each unit cell (Fig. 4f-h) shows that the multi-directional T phases are embedded within an R phase matrix, which is the characteristics of PNRs, with an overall state of multi-phase coexistence ('slush' polar state)⁶. The T₁ and T₂ oriented PNRs in *x* = 0.10 are in the size of 1–5 nm with small average polarizations (<10 pm) and a high polarization anisotropy (Fig. 4g, h). With further analyses, the distribution of T₁ and T₂ phases in a disordered matrix is clearly distinguished (Fig. 4h). The system is predominantly filled with low-angle PNR boundaries of no more than 30°, with relatively smooth transitions between these regions, consistent with the characteristics of PNRs. Our high-entropy strategy, which involves the incorporation of multiple elements with varying electronegativities and ionic sizes, enhances the formation and distribution of PNRs. This diverse elemental composition leads to a more complex energy landscape, which provides a stable dielectric response across a wide temperature range. We further discuss the electrical characteristics of the material in the following section.

Electrical microstructure and dielectric breakdown characteristics

The dielectric energy storage performance is highly associated with the electrical microstructure of the ceramic^{21,64}. Here, we demonstrate how our strategy of high entropy modulation impacts the electrical microstructure of the ceramics, and how it is associated with the transport behavior as well as the energy storage performances. First, the electrical core-shell structure of the ceramic and dielectric-electrode interface (DEI) is resolved based on methods described in our previous work²⁸. The fitted impedance responses are identical with the experimental values on the complex impedance plane, proving the successful fitting of the data (Supplementary Fig. 10a, c). The imaginary parts of modulus provide information on the capacitance of the different regions in the ceramic, which has a strong impact on the high field energy storage performance, thus is a focus of our discussions below.

The most significant trend extracted from the impedance response of NN-*x*CHZS ceramics is the enhancement of shell/grain boundary modulus with increasing *x*, which suggests that the thickness of insulating region in the ceramic is increased by an order of magnitude (Fig. 5a-d and Supplementary Fig. 11). This conclusion is not only based on the increase in shell modulus, but also on the fact that the permittivity of the regions of interest is on the same order of magnitude (Supplementary Fig. 12a and Supplementary Fig. 13). It should be noted that the scale bar of Fig. 5b is in a log scale (in comparison with the linear scale in Fig. 5d) for a better illustration to capture the frequency and temperature dependency of the shell electrical modulus of *x* = 0.00. Such electrical microstructural information reveals the reason behind the significant increase in E_b of the ceramic, which is the prerequisite for achieving the high energy storage performance. Moreover, the M'' peak in frequency spectrum of ceramic core (Fig. 5e) evolves from an asymmetric peak towards an ideal symmetrical Debye peak in *x* = 0.10, indicating the electrical microstructure becomes more homogenous, facilitating the homogeneous distribution of electric field within the ceramic and a high η during charge and discharge²⁸. The DEI modulus also increases with increasing *x*, suggesting the interface region between the ceramic and the electrode has a lower capacitance, and there is more electrical energy in the bulk crystal rather than in the DEI as *x* increase (Supplementary Fig. 12b). This proves that there are less mobile charge carriers at the DEI, which facilitate a more stable dielectric response and lower leakage current during operation. This is confirmed by the low dielectric loss shown across wide temperature range from -100 to 400 °C (Supplementary Fig. 13). As a result of the enhancements mentioned above, the impedance of the electrical components increases, leading to a 7.62-fold

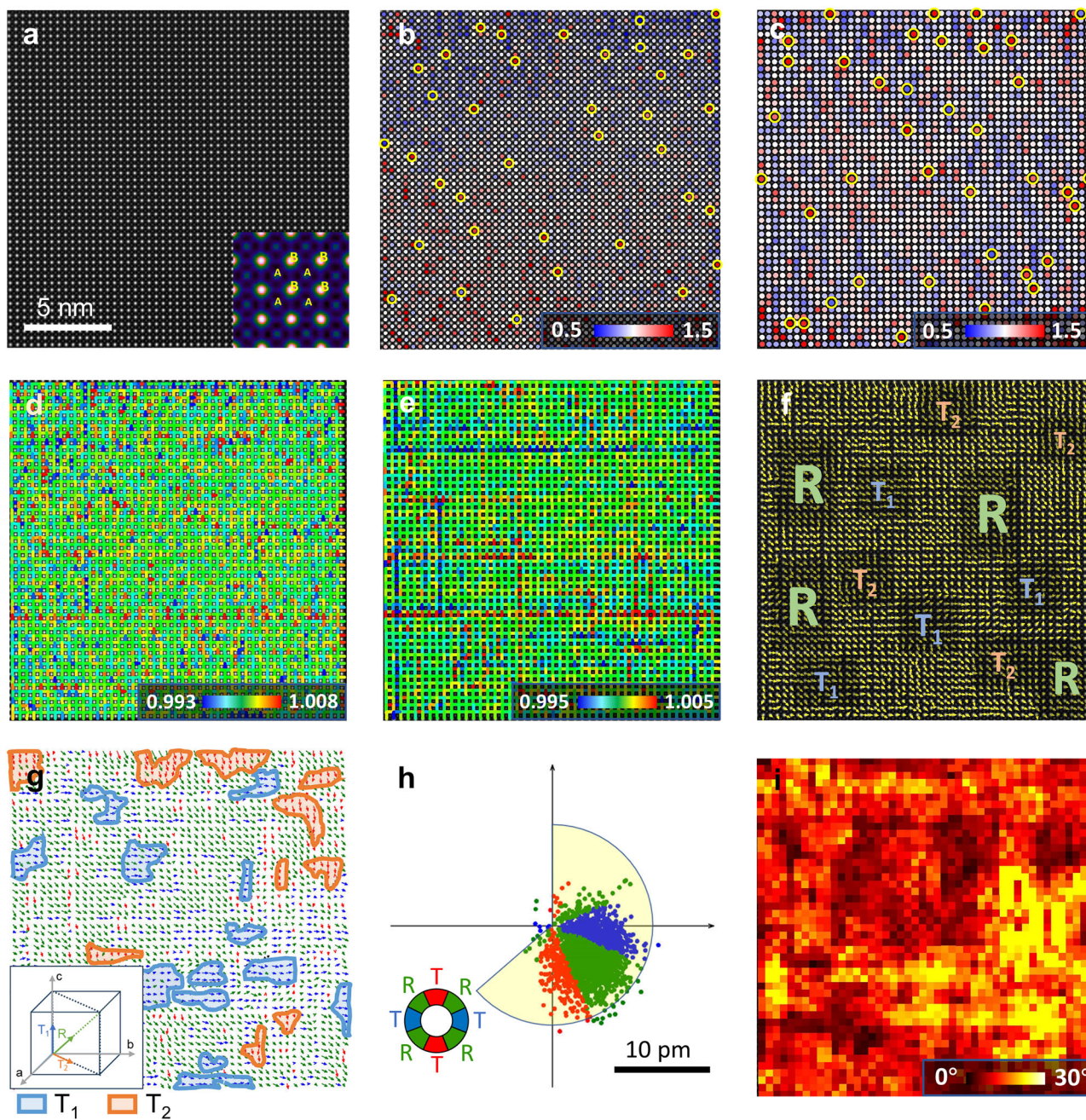


Fig. 4 | Atomic level microstructure and polarization configuration of $x = 0.10$. **a** HAADF-STEM atomic image along the $\langle 100 \rangle_c$ direction. Inset is a schematic for the relative position of A/B sites in perovskite structure. **b** Intensity mapping of A-sites. Regions with significant contrast fluctuations are marked with yellow circles, indicating possible element substitution ($\text{Ca}/\text{Sr} \rightarrow \text{Na}$) at these sites. **c** Intensity mapping of B-sites. Regions with significant contrast fluctuations are marked with yellow circles, indicating possible element substitution ($\text{Ti}/\text{Ta}/\text{Hf}/\text{Zr}/\text{Sn} \rightarrow \text{Nb}$) at these sites. **d** Lattice spacing mapping for A-site species, characterizing local lattice distortions associated with A-A bonds caused by doping. **e** Lattice spacing mapping for B-site species, characterizing local lattice distortions associated with B-B bonds caused by doping. **f** Atom displacement mapping with monochromatic arrows on

HAADF-STEM image background. **g** Extracted atomic displacement mapping with T_1 and T_2 polar nano regions (PNRs) indicated by blue and orange areas, respectively. Inset is a schematic of the polarization directions in the crystal structural coordinate system of $x = 0.10$. **h** Statistical atomic displacement distribution map for all polar vectors shown in (**g**). **i** Spatial distribution of relative angles of PNR directions. The values in the scale bars of (**b** and **c**) are the ratio of intensity of a specific site with respect to the statistical average intensity. The values in the scale bars of (**d** and **e**) are the ratio of the bond length of a specific bond with respect to the statistical average bond length. The spatial scale of (**b–g**) and (**i**) is the same as marked in (**a**).

rise in the total impedance value (Supplementary Fig. 10b). Besides, the activation energy (E_a) of charge carriers in the material shows a significant increase from 0.76 to 1.26 eV, suggesting that the conduction mechanism switch from extrinsic to intrinsic as x increase (Fig. 5f). Also, the transport barriers for charge carriers are significantly raised based on the increased E_a . These analyses prove the electrical

microstructural enhancement of NN-xCHZS and showcase the importance of electrical microstructure in developing high performance energy storage materials.

With the assistance of numerical simulation method, we push the E_b to a higher limit to achieve better energy storage performance⁶⁵. Through optimization of the microstructure of ceramic, we avoid

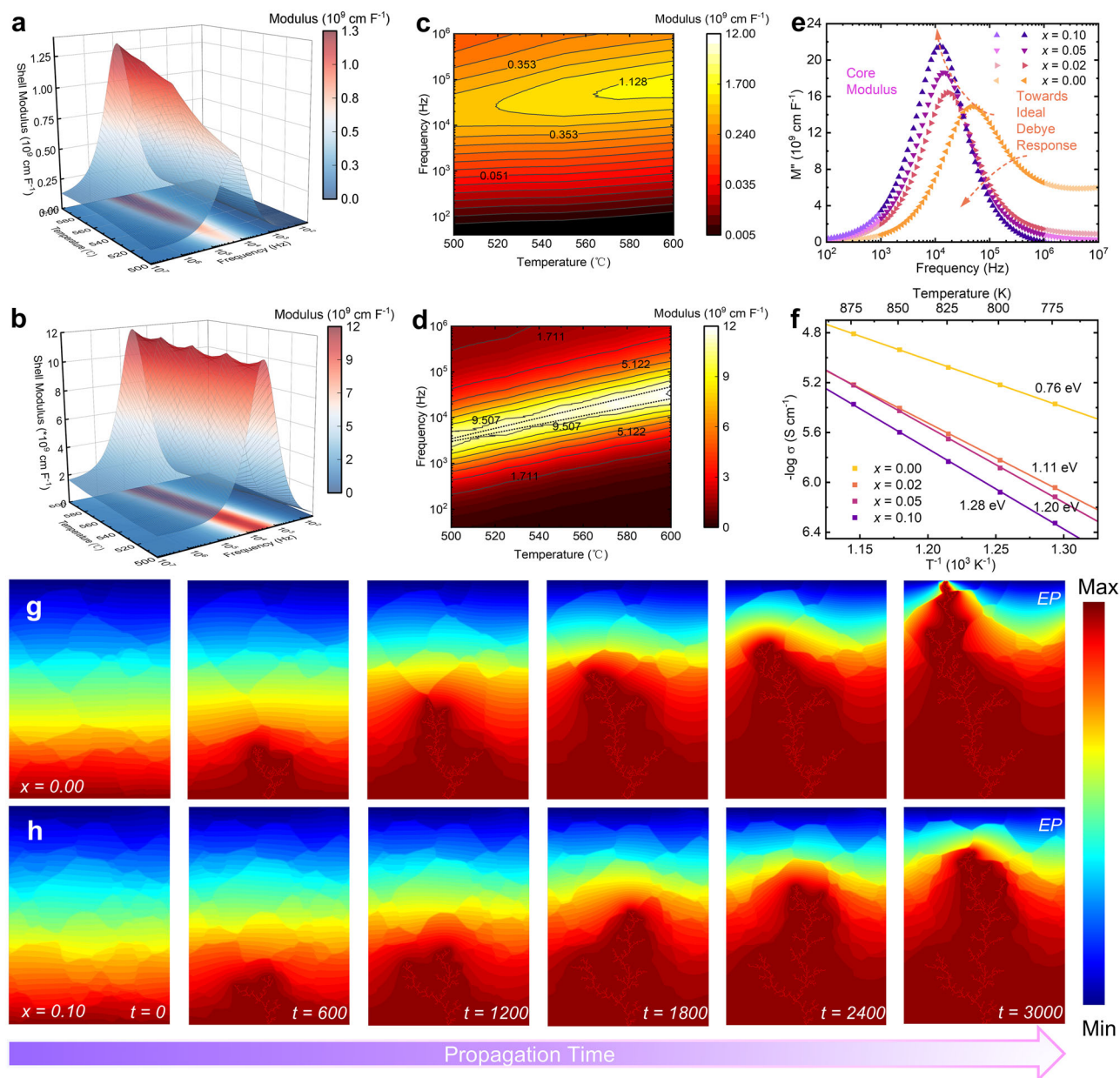


Fig. 5 | The electrical microstructure, associated transport behavior and dielectric breakdown behavior of NN-xCHZS ceramic. Frequency and temperature dependency of shell modulus for (a) $x = 0.00$ and (b) $x = 0.10$. Shell modulus mapping of (c) $x = 0.00$ and (d) $x = 0.10$. e Evolution of core modulus with x at 525 °C. f Arrhenius plot of the thermal activation process for carrier transport in

NN-xCHZS. The simulated temporal evolution of breakdown behavior for (g) $x = 0.00$ and (h) $x = 0.10$ shown in electric potential (EP) mappings. The min and max values are 0 and 2.1 kV, respectively. The simulation is conducted with discretized time steps of fixed lengths. Step number for the displayed frame are labelled with inset text.

breakdown of the dielectric during operation and increase its working voltage⁶⁶. The microstructure of NN-xCHZS is denser with increasing x , and shows no pores for $x = 0.10$ ceramic based on both scanning electron microscopy (SEM) and optical microscopy (Supplementary Figs. 14 and 15). For accurate description of the material, we construct the area of simulation based on actual SEM images of the samples (Supplementary Fig. 16). The dielectric permittivity of the grain and grain boundary are considered when solving the electrostatic equilibrium equation and path probability equation (supporting information)^{67,68}. These equations are solved in a step-wise manner until the far edge of electrical tree propagate through the area of simulation. As a result, the electrical tree pattern and temporal evolution of the electrical breakdown of NN-xCHZS ceramic are visualized and compared. Due to the insulating nature of our material, branch-

type breakdown channels are present rather than ivy-type channels⁶⁹. The simulation provides a visualization for the high E_b of $x = 0.10$ than that of $x = 0.00$ based on their dielectric characteristics, proving the success of our high entropy modulation strategy. The breakdown path in $x = 0.10$ only propagated 84% through the simulated area when $x = 0.00$ has already experienced total electrical breakdown at $t = 3000$ (Fig. 5g, h and Supplementary Fig. 17). The electric field is concentrated in the region where the breakdown paths have not reached, due to the large difference in resistivities of the electrical tree and the ceramic body. The high E_b is contributed by the more homogeneous distribution of electric potential across the electrical microstructure of NN-xCHZS (Fig. 5e). The highly resistive grain boundaries serve as barriers hindering the propagation of breakdown channels across the ceramic. With higher grain boundary density, the

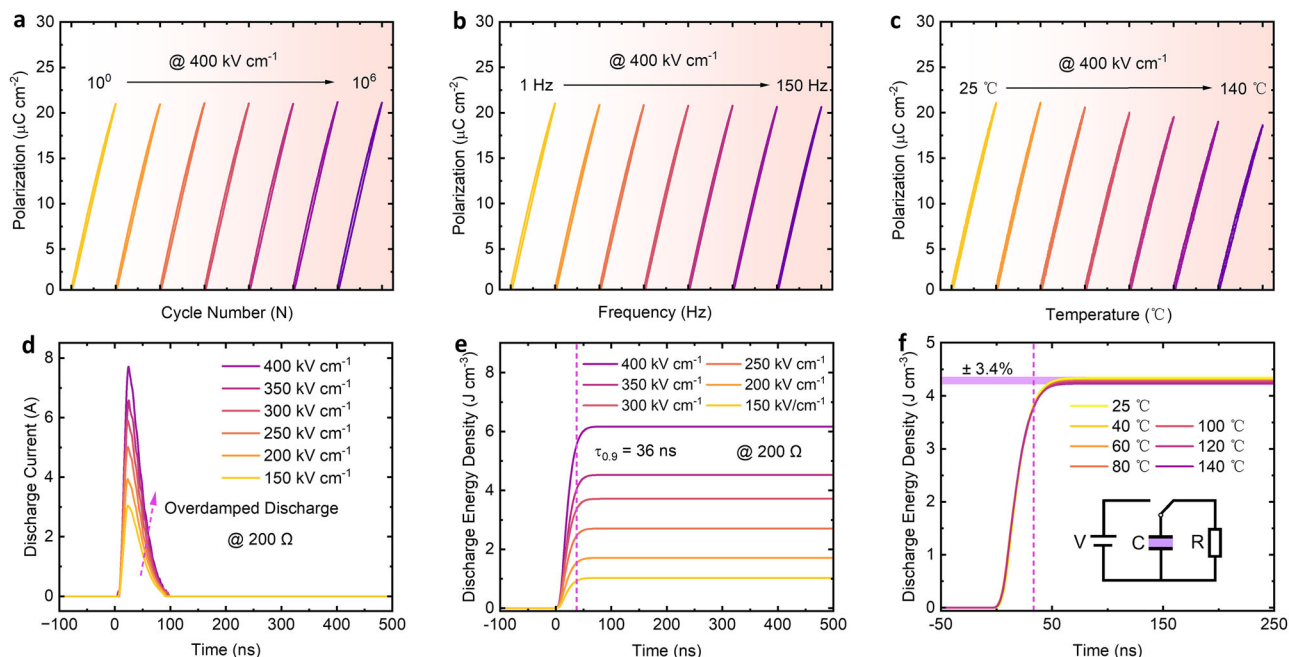


Fig. 6 | The stability, fatigue and discharge performance of $x = 0.10$. **a** Anti-fatigue performance up to 10^6 cycles. **b** Frequency stability from 1 Hz to 150 Hz. **c** Temperature stability from 25 °C to 140 °C. **d** Discharge current towards a 200 Ω load. **e** Discharge energy density (W_{dis}) integrated from discharge current.

f Temperature stability of W_{dis} from 25 °C to 140 °C. Inset is a schematic of the charge-discharge circuit setup with a metal-insulator-metal (MIM) electrostatic capacitor made from $x = 0.10$ as discharge component.

breakdown time is effectively delayed. We have demonstrated here by both experiments and numerical simulation the importance of electrical microstructure in achieving high energy storage performance of dielectric ceramics, and demonstrated a successful manipulation of electrical microstructure in NN based material, providing a new dimension of optimization for developing novel energy storage dielectric materials.

Stability, fatigue and discharge performance

Stability during the charge-discharge cycle and anti-fatigue property after long period of operation are crucial for energy storage dielectrics in practical application. For $x = 0.10$, the sample maintained steady functionality even after 1 million cycles (Fig. 6a and Supplementary Fig. 18a). A high η over 90% suggests almost no degradation of the material property after the long cycles. An outstanding frequency stability is shown between 1 Hz and 150 Hz (Fig. 6b and Supplementary Fig. 18b), with an increase in η which is an indication of multiple polarization mechanisms in the material⁷⁰. With the increase in frequency, some of the slow polarization mechanisms such as the space charge polarization cannot follow the fast switching of applied electric field and hence results in a higher η (lower loss due to reduced reorientation of space charge polarization). Since these relaxor compositions are operating above their Curie temperatures, the permittivity drops with increasing temperature, which may be the primary reason for the decrease in polarization, and as a result, W_{rec} in $x = 0.10$ drops with increasing temperature (Fig. 6c and Supplementary Fig. 18c). However, η shows little degradation up to 140 °C. These results indicate that NN- x CHZS ceramics are suitable for long term operation in electrical and electronic devices.

An NN- x CHZS based metal-insulator-metal (MIM) capacitor is then placed in a charge-discharge circuit to examine its potential of operation in circuit (Fig. 6f inset). An electromagnetic induction probe was used to collect the current signal during the discharge without direct contact with the discharge circuit, thus avoiding direct interference and ensure an accurate measurement. The capacitor is able to subject to high electric field of 400 kV cm⁻¹, and shows a fast discharge

rate to a 200 Ω resistor with 90% of electrical energy released within 36 ns (Fig. 6d, e). The capacitor shows overdamped discharge at all measured field strengths. Based on the discharge measurement, the W_{dis} shows little variation of 3.4% across a wide temperature range from 25 °C to 140 °C (Fig. 6f). These results demonstrate the practical performance of NN- x CHZS in an RC discharge circuit, verifying the reliability of the material as energy storage dielectric.

In conclusion, we have proposed a high entropy modulation technique, which stabilizes the high field dielectric response of the quantum paraelectric matrix, and has achieved excellent energy storage performance in the bulk dielectric perovskite. The atomic level polarization configuration is optimized with domains smaller than 5 nm to provide high response speed towards electric field. The high degree of long-range oxygen octahedron tilting provides energy reservoir for the large capacitive energy storage. The electrical microstructure is enhanced by an order of magnitude for reduced transport behavior, which, in conjunction with the band structure optimization, provides a large E_b at high electric field. Finally, the stability and discharge reliability are confirmed by applying NN- x CHZS based capacitor in a RC discharge circuit. This work provides a novel pathway to synergistic optimization of the polar configuration, electrical microstructure and band structure to develop next generation high performance energy storage dielectrics, for applications in EVs and other electrical systems. Our work is expected to stimulate more efforts in this area and push the discovery of new energy storage dielectrics.

Methods

Sample preparation

$(0.75-x)\text{NaNbO}_3 \cdot 0.10\text{NaTaO}_3 \cdot 0.15\text{SrTiO}_3 \cdot x\text{Ca}(\text{Hf}_{x/3}\text{Zr}_{x/3}\text{Sn}_{x/3})\text{O}_3$ (NN- x CHZS; $x = 0.00, 0.02, 0.05, 0.10$) ceramics were synthesized via solid state reaction method with high purity raw materials of Na_2CO_3 (International Laboratory USA, 99.95%), Nb_2O_5 (Sinopharm, 99.5%), CaCO_3 (International Laboratory USA, 99.5%), SrCO_3 (Aladdin, 99.95%), TiO_2 (Aladdin, 99.5%), SnO_2 (Aladdin, 99.5%), Ta_2O_5 (International Laboratory USA, 99.99%), HfO_2 (Aladdin, 99.95%),

and ZrO_2 (Sinopharm, 99.5%). These raw materials were weight stoichiometrically and mixed with planetary ball milling for 24 h, then calcined for 3 h at 900 °C. The calcined powders were hand milled for 30 min before planetary milling for another 24 h. Then, 0.5 wt% polyvinyl alcohol solution was added to the powder to facilitate pellet forming. The powders were pressed into 1-mm-thick pellet and sintered at 1250–1350 °C to obtain dense samples. Pellets are buried in sacrificial powder during sintering to avoid volatilization during sintering.

Structural characterizations

XRD data was collected with X-ray diffractometer (D8, Bruker, Germany) with $\text{Cu-K}\alpha 1$ (1.5406 Å) radiation. Morphologies of the samples were examined with a scanning electron microscope (Nova Nano-SEM450, FEI, USA) and an optical microscope (DFC450, Leica, Germany). The band structure is evaluated with a UV-vis spectrometer (Lambda 1050, PerkinElmer, USA). The specimens for atomic-resolution scanning transmission electron microscopy (AC-STEM) were prepared by mechanical thinning, ultrasonic cutting, and Ar-ion thinning until electrons can penetrate the samples with a thickness below 100 nm. High-resolution grain/domain imaging and SAED patterns were acquired using a JEM-ARM300F2 microscope in TEM mode. Atomic-scale high-angle annular dark-field (HAADF) images were obtained in STEM mode. Quantitative analysis, including contrast evaluation, lattice spacing mapping, atomic displacement (polarization), and domain angle determination, was performed using customized program written in C++ and Qt software. X-ray photoelectron spectroscopy analysis was conducted with an X-ray Photoelectron Spectrometer (ESCALAB 250Xi, Thermo Scientific, USA).

Electrical characterizations

Before high voltage measurement, Au electrodes with 1 mm in diameter were sputtered on the samples of ~0.1 mm in thickness. Ferroelectric hysteresis loops and leakage current were measured with a ferroelectric tester (Precision Multiferroic II, Radiant Technologies, USA). Breakdown information is analyzed with Weibull distribution function, of which details are in the Supporting Information. Dielectric data and impedance spectra were collected with a precision impedance analyzer (4294 A, Agilent, USA). Discharge measurement was conducted on a commercial charge/discharge platform (CFD-003, TG Technology, China).

Density function theory (DFT) calculation

The first-principles calculations based on density functional theory (DFT) were carried out on Vienna Ab-initio Simulation Package (VASP.5.4.4.18)⁷¹. The generalized gradient approximation was applied with Perdew–Burke–Ernzerhof functional for the exchange–correlation effects, and the ionic potentials were treated by projector augmented wave approximation^{72,73}. Pristine NaNbO_3 (NNO) and NNO-based oxides ($\text{Na}_{1-x-z}\text{Sr}_x\text{Ca}_z\text{Nb}_{1-x-y-z}\text{Ti}_x\text{Ta}_y\text{M}_z\text{O}_3$, $\text{M}=\text{Hf}$, Zr , Sn ; $x=0, 0.15$; $y=0, 0.1$; $z=0, 0.1$) were modeled by using $2 \times 2 \times 3$ supercell with all atoms relaxed. The $3 \times 3 \times 2$ Monkhorst-Pack k -points meshes were used for the integration of the Brillouin zone⁷⁴. During all calculations, a cutoff energy of 400 eV was used for the plane-wave expansion. All structures were fully relaxed with the residual forces on atoms below 0.02 eV/Å.

Finite element simulation

The evolution of electric tree during breakdown of the samples is simulated with 2D model in COMSOL 5.5 software. For accurate description of the physical parameters governing the breakdown process and electric field distribution, MATLAB is used to construct the physical model and field configuration. Details of the physical model and equations are described in the Supporting Information.

Data availability

Data sets generated during the current study are available from the corresponding author on reasonable request.

References

- Wang, Y., Robson, M. J., Manzotti, A. & Ciucci, F. High-entropy perovskites materials for next-generation energy applications. *Joule* **7**, 848–854 (2023).
- Han, S. et al. High energy density in artificial heterostructures through relaxation time modulation. *Science* **384**, 312–317 (2024).
- Pan, H. et al. Ultrahigh energy storage in superparaelectric relaxor ferroelectrics. *Science* **374**, 100–104 (2021).
- Liu, Y. et al. Phase-field simulations of tunable polar topologies in lead-free ferroelectric/paraelectric multilayers with ultrahigh energy-storage performance. *Adv. Mater.* **34**, 2108772 (2022).
- Yang, L. et al. Perovskite lead-free dielectrics for energy storage applications. *Prog. Mater. Sci.* **102**, 72–108 (2019).
- Shu, L. et al. Partitioning polar-slush strategy in relaxors leads to large energy-storage capability. *Science* **385**, 204–209 (2024).
- Cheema, S. S. et al. Giant energy storage and power density negative capacitance superlattices. *Nature* **629**, 803–809 (2024).
- Yang, B. et al. Engineering relaxors by entropy for high energy storage performance. *Nat. Energy* **8**, 956–964 (2023).
- Yang, B. et al. High-entropy enhanced capacitive energy storage. *Nat. Mater.* **21**, 1074–1080 (2022).
- Tian, H. et al. Disorder-tuned conductivity in amorphous monolayer carbon. *Nature* **615**, 56–61 (2023).
- Zhang, M. et al. Ultrahigh energy storage in high-entropy ceramic capacitors with polymorphic relaxor phase. *Science* **384**, 185–189 (2024).
- Yang, M. et al. Polymer nanocomposite dielectrics for capacitive energy storage. *Nat. Nanotechnol.* **19**, 588–603 (2024).
- Yang, M. et al. Roll-to-roll fabricated polymer composites filled with subnanosheets exhibiting high energy density and cyclic stability at 200 °C. *Nat. Energy* **9**, 143–153 (2024).
- Jayakrishnan, A. R. et al. Are lead-free relaxor ferroelectric materials the most promising candidates for energy storage capacitors? *Prog. Mater. Sci.* **132**, 101046 (2023).
- Zheng, H. et al. Heterogeneous field response of hierarchical polar laminates in relaxor ferroelectrics. *Science* **384**, 1447–1452 (2024).
- Liu, L. et al. Size and orientation of polar nanoregions characterized by PDF analysis and using a statistical model in a $\text{Bi}(\text{Mg}1/2\text{Ti}1/2)\text{O}_3\text{-PbTiO}_3$ ferroelectric re-entrant relaxor. *J. Mater. Chem. A* **12**, 11580–11590 (2024).
- Bencan, A. et al. Atomic scale symmetry and polar nanoclusters in the paraelectric phase of ferroelectric materials. *Nat. Commun.* **12**, 3509 (2021).
- Long, C. et al. Excellent energy storage properties with ultrahigh Wrec in lead-free relaxor ferroelectrics of ternary $\text{Bi}_0.5\text{Na}_0.5\text{TiO}_3\text{-SrTiO}_3\text{-Bi}_0.5\text{Li}_0.5\text{TiO}_3$ via multiple synergistic optimization. *Energy Storage Mater.* **65**, 103055 (2024).
- Gao, Y. et al. Ultrahigh energy storage in tungsten bronze dielectric ceramics through a weakly coupled relaxor design. *Adv. Mater.* **36**, 2310559 (2024).
- Chen, X. et al. Programming polarity heterogeneity of energy storage dielectrics by bidirectional intelligent design. *Adv. Mater.* **36**, 2311721 (2024).
- Wang, G. et al. Electroceramics for high-energy density capacitors: current status and future perspectives. *Chem. Rev.* **121**, 6124–6172 (2021).
- Schweidler, S. et al. High-entropy materials for energy and electronic applications. *Nat. Rev. Mater.* **9**, 266–281 (2024).
- Lin, P. et al. An integral droop for transient power allocation and output impedance shaping of hybrid energy storage system in DC microgrid. *IEEE Trans. Power Electron.* **33**, 6262–6277 (2018).

24. Qu, D. et al. Electrochemical impedance and its applications in energy-storage systems. *Small Methods* **2**, 1700342 (2018).
25. Irvine, J. T. S., Sinclair, D. C. & West, A. R. Electroceramics: characterization by impedance spectroscopy. *Adv. Mater.* **2**, 132–138 (1990).
26. Li, M. et al. A family of oxide ion conductors based on the ferroelectric perovskite NaO.5BiO.5TiO_3 . *Nat. Mater.* **13**, 31–35 (2014).
27. Maradesa, A. et al. Advancing electrochemical impedance analysis through innovations in the distribution of relaxation times method. *Joule* **8**, 1958–1981 (2024).
28. Fan, Y. et al. Pb, Bi, and rare earth free X6R barium titanate–sodium niobate ceramics for high voltage capacitor applications. *Appl. Phys. Lett.* **122**, 143901 (2023).
29. Yang, H. et al. Novel BaTiO_3 -Based, Ag/Pd-compatible lead-free relaxors with superior energy storage performance. *ACS Appl. Mater. Interfaces* **12**, 43942–43949 (2020).
30. Lim, K., Popovic, J. & Maier, J. Ion transport and growth behavior of solid electrolyte interphases on Li and Na with liquid electrolytes based on impedance analysis. *J. Mater. Chem. A* **11**, 5725–5733 (2023).
31. Yang, W., Moehl, T., Service, E. & Tilley, S. D. Operando analysis of semiconductor junctions in multi-layered photocathodes for solar water splitting by impedance spectroscopy. *Adv. Energy Mater.* **11**, 2003569 (2021).
32. Ha, K.-H. et al. Highly sensitive capacitive pressure sensors over a wide pressure range enabled by the hybrid responses of a highly porous nanocomposite. *Adv. Mater.* **33**, 2103320 (2021).
33. Kim, S. H. et al. Strain-invariant stretchable radio-frequency electronics. *Nature* **629**, 1047–1054 (2024).
34. Zhang, M.-H. et al. Tailoring high-energy storage NaNbO_3 -based materials from antiferroelectric to relaxor states. *Nat. Commun.* **14**, 1525 (2023).
35. Randall, C. A., Fan, Z., Reaney, I., Chen, L. Q. & Trolier-McKinstry, S. Antiferroelectrics: history, fundamentals, crystal chemistry, crystal structures, size effects, and applications. *J. Am. Ceram. Soc.* **104**, 3775–3810 (2021).
36. Qi, H. et al. Large (anti)ferrodistortive NaNbO_3 -based lead-free relaxors: polar nanoregions embedded in ordered oxygen octahedral tilt matrix. *Mater. Today* **60**, 91–97 (2022).
37. Luo, N. et al. Well-defined double hysteresis loop in NaNbO_3 antiferroelectrics. *Nat. Commun.* **14**, 1776 (2023).
38. Hwang, W., Kim, K., Oh, S.-H. V. & Soon, A. Insights into enhanced antiferroelectricity in doped-niobate perovskites for high energy-storage density applications. *Nano Energy* **128**, 109791 (2024).
39. Aso, S., Matsuo, H. & Noguchi, Y. Reversible electric-field-induced phase transition in Ca-modified NaNbO_3 perovskites for energy storage applications. *Sci. Rep.* **13**, 6771 (2023).
40. Stella, F. et al. Design and Testing of an Automotive Compliant 800V 550 kVA SiC Traction Inverter with Full-Ceramic DC-Link and EMI Filter In 2022 *IEEE Energy Conversion Congress and Exposition (ECCE)*. pp. 1–8 (IEEE, Detroit, MI, USA, 2022).
41. Wang, S., Hattori, A., Ozeki, Y. & Ogawa, H. Development of Multi-layered SrTiO_3 Thin-Film Capacitors For Embedded Passive Applications In 2007 *Sixteenth IEEE International Symposium on the Applications of Ferroelectrics*. 484–486 (IEEE, Nara, Japan, 2007).
42. Lu, Z. et al. Superior energy density through tailored dopant strategies in multilayer ceramic capacitors. *Energy Environ. Sci.* **13**, 2938–2948 (2020).
43. Cao, W. et al. Phase and band structure engineering via linear additive in NBT-ST for excellent energy storage performance with superior thermal stability. *ACS Appl. Mater. Interfaces* **14**, 54051–54062 (2022).
44. Luo, N. et al. Constructing phase boundary in AgNbO_3 antiferroelectrics: pathway simultaneously achieving high energy density and efficiency. *Nat. Commun.* **11**, 4824 (2020).
45. Ma, L. et al. High energy storage density in NaNbO_3 antiferroelectrics with double hysteresis loop. *J. Mater.* **10**, 1026–1035 (2023).
46. Lee, H., Kim, J. R., Lanagan, M. J., Trolier-McKinstry, S. & Randall, C. A. High-energy density dielectrics and capacitors for elevated temperatures: $\text{Ca}(\text{Zr,Ti})\text{O}_3$. *J. Am. Ceram. Soc.* **96**, 1209–1213 (2013).
47. Ang, C., Bhalla, A. S. & Cross, L. E. Dielectric behavior of paraelectric KTaO_3 , CaTiO_3 , and $(\text{Ln}_{1/2}\text{Na}_{1/2})\text{TiO}_3$ under a dc electric field. *Phys. Rev. B* **64**, 184104 (2001).
48. Nova, T. F., Disa, A. S., Fechner, M. & Cavalleri, A. Metastable ferroelectricity in optically strained SrTiO_3 . *Science* **364**, 1075–1079 (2019).
49. Zhang, P. et al. Intrinsic-strain-induced ferroelectric order and ultrafine nanodomains in SrTiO_3 . *Proc. Natl. Acad. Sci. USA* **121**, e2400568121 (2024).
50. Li, X. et al. Terahertz field-induced ferroelectricity in quantum paraelectric SrTiO_3 . *Science* **364**, 1079–1082 (2019).
51. Divilov, S. et al. Disordered enthalpy–entropy descriptor for high-entropy ceramics discovery. *Nature* **625**, 66–73 (2024).
52. Huang, H., Sun, C. Q., Tianshu, Z. & Hing, P. Grain-size effect on ferroelectric $\text{Pb}(\text{Zr}_{1-x}\text{Ti}_x)\text{O}_3$ solid solutions induced by surface bond contraction. *Phys. Rev. B* **63**, 184112 (2001).
53. Cittanti, D. et al. Analysis, design, and experimental assessment of a high power density ceramic DC-link capacitor for a 800 V 550 kVA electric vehicle drive inverter. *IEEE Trans. Ind. Appl.* **59**, 7078–7091 (2023).
54. Chen, L. et al. Large energy capacitive high-entropy lead-free ferroelectrics. *Nano-Micro Lett.* **15**, 65 (2023).
55. Johnston, K. E. et al. The polar phase of NaNbO_3 : a combined study by powder diffraction, solid-state NMR, and first-principles calculations. *J. Am. Chem. Soc.* **132**, 8732–8746 (2010).
56. Kim, J. et al. Ultrahigh capacitive energy density in ion-bombarded relaxor ferroelectric films. *Science* **369**, 81–84 (2020).
57. Müller, K. A. & Burkard, H. SrTiO_3 : an intrinsic quantum paraelectric below 4 K. *Phys. Rev. B* **19**, 3593–3602 (1979).
58. Chandra, P., Lonzarich, G. G., Rowley, S. E. & Scott, J. F. Prospects and applications near ferroelectric quantum phase transitions: a key issues review. *Rep. Prog. Phys.* **80**, 112502 (2017).
59. Rowley, S. E. et al. Ferroelectric quantum criticality. *Nat. Phys.* **10**, 367–372 (2014).
60. Fechner, M. et al. Quenched lattice fluctuations in optically driven SrTiO_3 . *Nat. Mater.* **23**, 363–368 (2024).
61. Landau, L. D. On the theory of phase transitions. *Zh. eksp. teor. Fiz.* **7**, 926 (1937).
62. Lin, B. et al. Ultrahigh electromechanical response from competing ferroic orders. *Nature* **633**, 798–803 (2024).
63. Yoneda, Y. et al. Local and electronic structures of NaNbO_3 , AgNbO_3 , and KNbO_3 . *Jpn. J. Appl. Phys.* **63**, 09SP12 (2024).
64. Zhang, L., Pu, Y. & Chen, M. Complex impedance spectroscopy for capacitive energy-storage ceramics: a review and prospects. *Mater. Today Chem.* **28**, 101353 (2023).
65. Khondabi, M., Ahmadvand, H. & Javanbakht, M. Revisiting the dielectric breakdown in a polycrystalline ferroelectric: a phase-field simulation study. *Adv. Theory Simul.* **6**, 2200314 (2023).
66. Wang, J. et al. Texture engineering modulating electromechanical breakdown in multilayer ceramic capacitors. *Adv. Sci.* **10**, 2300320 (2023).
67. Huang, Y. H. et al. From core–shell BaO.4SrO.6TiO_3 @ SiO_2 particles to dense ceramics with high energy storage performance by spark plasma sintering. *J. Mater. Chem. A* **6**, 4477–4484 (2018).
68. Gao, S. et al. Ultrahigh energy density and excellent discharge properties in Ce^{4+} and Ta^{5+} co-modified AgNbO_3 relaxor antiferroelectric ceramics via multiple design strategies. *Acta Materialia* **246**, 118730 (2023).

69. Sturge, K. M. et al. Dynamics of high-speed electrical tree growth in electron-irradiated polymethyl methacrylate. *Science* **385**, 300–304 (2024).
70. Wang, B. et al. High-k gate dielectrics for emerging flexible and stretchable electronics. *Chem. Rev.* **118**, 5690–5754 (2018).
71. Kresse, G. & Furthmüller, J. Efficient iterative schemes for ab initio total-energy calculations using a plane-wave basis set. *Phys. Rev. B* **54**, 11169–11186 (1996).
72. Perdew, J. P., Burke, K. & Ernzerhof, M. Generalized gradient approximation made simple. *Phys. Rev. Lett.* **77**, 3865–3868 (1996).
73. Kresse, G. & Joubert, D. From ultrasoft pseudopotentials to the projector augmented-wave method. *Phys. Rev. B* **59**, 1758–1775 (1999).
74. Monkhorst, H. J. & Pack, J. D. Special points for Brillouin-zone integrations. *Phys. Rev. B* **13**, 5188–5192 (1976).
75. Peng, H. et al. High-entropy relaxor ferroelectric ceramics for ultrahigh energy storage. *Nat. Commun.* **15**, 5232 (2024).

Acknowledgements

Y.F., W.Q., H.Q., and S.G. contributed equally to this work. This work was supported by the National Key R&D Program of China (2021YFB3201100), the Science and Technology Program of Guangdong Province of China (2021B1515130010) and Shenzhen Science and Technology Program (JCYJ20240813162024031). The authors thank Mr. Chuansheng Ma from the Instrument Analysis Center of Xi'an Jiaotong University for the assistance of aberration-corrected STEM.

Author contributions

Y.F. and H.H. conceived the idea of this work and designed the experiments. H.H. and H.W. supervised the work, H.F. provided resource support. Y.F. prepared the material and conducted electrical measurement. H.W. supervised the structural measurement which W.Q., Y.F., Y.Y., and Y.Z. conducted. H.Q., S.G., and Lu.L. conducted calculation and simulation. S.Y., Z.L., J.Y., S.L., L.W., H.L., and Lin.L. provided support for characterization. Y.F. drafted the first version of the manuscript. All authors discussed and revised the manuscript.

Competing interests

The authors declare no conflict of interest.

Additional information

Supplementary information The online version contains supplementary material available at <https://doi.org/10.1038/s41467-025-59081-x>.

Correspondence and requests for materials should be addressed to Haijun Wu or Haitao Huang.

Peer review information *Nature Communications* thanks Abhishek Sasmal, Muhammad Sheeraz, and the other, anonymous, reviewer(s) for their contribution to the peer review of this work. A peer review file is available.

Reprints and permissions information is available at <http://www.nature.com/reprints>

Publisher's note Springer Nature remains neutral with regard to jurisdictional claims in published maps and institutional affiliations.

Open Access This article is licensed under a Creative Commons Attribution-NonCommercial-NoDerivatives 4.0 International License, which permits any non-commercial use, sharing, distribution and reproduction in any medium or format, as long as you give appropriate credit to the original author(s) and the source, provide a link to the Creative Commons licence, and indicate if you modified the licensed material. You do not have permission under this licence to share adapted material derived from this article or parts of it. The images or other third party material in this article are included in the article's Creative Commons licence, unless indicated otherwise in a credit line to the material. If material is not included in the article's Creative Commons licence and your intended use is not permitted by statutory regulation or exceeds the permitted use, you will need to obtain permission directly from the copyright holder. To view a copy of this licence, visit <http://creativecommons.org/licenses/by-nc-nd/4.0/>.

© The Author(s) 2025